FirePhysChem 3 (2023) 217–226

Contents lists available at ScienceDirect

FirePhysChem

journal homepage: http://www.keaipublishing.com/cn/journals/firephyschem/

Thermal decomposition kinetics and combustion performance of paraffin-based fuel in the presence of CeO_2 catalyst

Yash Pal[a,*], Sri Nithya Mahottamananda[b], Subha S[a], Sasi Kiran Palateerdham[c], Antonella Ingenito[c]

[a] School of Aeronautical Sciences, Hindustan Institute of Technology and Science, Chennai, 603103, India
[b] Department of Aerospace Engineering, BS Abdur Rahman Crescent Institute of Science & Technology, Chennai, 600048, India
[c] School of Aerospace Engineering, University of Rome "La Sapienza", 00138, Rome, Italy

ARTICLE INFO

Keywords:
Paraffin wax
CeO_2
Thermal decomposition
Catalysis
Regression rate

ABSTRACT

In recent years, significant developments have been made in solid-fuel combustion. Paraffin-based fuels could be a potential solid fuel for hybrid and ramjet applications due to their high regression rate, low cost, and minimal environmental impact. This study examines the thermal and combustion performance of paraffin-based fuels loaded with CeO_2 combustion catalysts and Al additive. A typical melt-cast technique was used to prepare three different fuel formulations, which are paraffin/10 wt.% of Al (S2), paraffin/10 wt.% of CeO_2 (S3), and CeO_2-Al (10:10 wt.%) binary composite (S4). The pure paraffin (S1) fuel was manufactured as a reference formulation. The CeO_2-Al binary composite powder was prepared by ball-milling of CeO_2 and Al powders. The CeO_2 and Al nanoparticles were characterized by X-ray diffraction (XRD), particle size distribution (PSD), and scanning electron microscope (SEM). The PSD study revealed that the majority of CeO_2, Al, and CeO_2-Al binary composite particles are 29 nm, 34 nm, and 26 nm in size, respectively. The thermogravimetric analysis (TGA) was used to investigate the effect of CeO_2 and Al on the thermal decomposition of paraffin. The results indicate that the paraffin decomposes faster and at a higher rate when CeO_2 and CeO_2-Al binary composite additives were added. The activation energy of paraffin-based fuel (S4) was reduced from 254 kJ/mol to 214 kJ/mol when a CeO_2-Al combustion catalyst was added. The lab-scale ballistic tests showed that the average regression rate of paraffin-Al (S2) and paraffin-CeO_2(S3) samples increased in the range of 1.1-1.4 mm/s and 1.12-1.38 mm/s, respectively, whereas, with the CeO_2-Al binary composite (S4) sample, a reasonable improvement of 1.15 mm/s to 1.49 mm/s was reported.

1. Introduction

The term "hybrid rocket motor" (HRM) refers to a promising chemical propulsion technology that uses propellants in different phases, the most prevalent of which are solid fuel and liquid oxidizer [1–3]. Due to different phases of propellant, HRM holds several advantages such as inherent safety, high reliability, minimal environmental impact, thrust modulation, and low development cost. However, the low regression rate and poor combustion efficiency of polymeric fuels such as hydroxyl-terminated polybutadiene (HTPB), polymethyl methacrylate (PMMA), and polyethylene (PE) used in HRM are the main drawbacks limiting their applications [4–9]. The motor operating conditions and composition of the solid fuel can strongly affect the fuel regression rate, which is considered a vital motor design parameter. Several techniques, such as solid fuel loaded with energetic additives [3,4,10–15], non-conventional fuel geometries [16–24], and changing the fluid dynamics of oxidizer injection [2,25–30], have been developed to improve the fuel regression rate. Paraffin-based fuels have been studied as a high regression fuel due to their low cost, reduced complexity, and increased performance. According to Karabeyoglu et al.[31], the paraffin-based fuels reported a 3–4 times higher regression rate than the classical polymer-based fuels. A technical grade paraffin wax is saturated hydrocarbons with low molecular weight and a melting point ranging from 45 °C to 72 °C [32,33]. During the combustion process in HRM, low viscosity and surface tension melting layer forms on the burning surface, and droplet entrainment of melt paraffin occurs under the influence of high-speed oxidizer flow. The additional mass entrainment of paraffin droplets into the combustion zone is responsible for the high regression rate of fuel. As a result, paraffin has the most significant potential to be the best solid fuel for HRM [34].

For liquefying hybrids, the combustion reactions mainly occur in the turbulent boundary layer, and much more fuel can be entrained into the combustion zone before being vaporized. However, our previous studies

* Corresponding author.
E-mail addresses: yashpal@hindustanuniv.ac.in, yashsoni06@gmail.com (Y. Pal).

https://doi.org/10.1016/j.fpc.2022.10.005
Received 12 July 2022; Received in revised form 11 October 2022; Accepted 21 October 2022
Available online 23 October 2022

found that paraffin did not undergo complete combustion despite controlled vaporization into the combustion zone [7,35]. Since paraffin has a low melting point and poor mechanical properties, which restricts its use in the chemical propulsion system, subsequently vibrations and impact loads during manufacturing, transportation, storage, and operation can break up and collapse fuel grain structures. The combustion reactions in hybrid rocket combustion take place mainly in the turbulent boundary layer located above the burning surface, and the regression rate is largely determined by the flow of oxidizer and the heat feedback from the high-temperature flame to the burning fuel surface. The distance between the burning fuel surface and the combustion flame will decrease if some burning catalysts accelerate oxidation reactions, and then the regression rate will increase due to increased heat feedback [36–40]. The increased heat feedback from the flame surface makes these active catalysts more efficient at decomposing paraffin fuel and improving its regression rate.

Several studies reported thermal and decomposition kinetics of paraffin under N_2, O_2, and Ar environments [39–42]. Jaw et al. [41] evaluated the kinetic parameters of thermal decomposition using non-isothermal DTA/TGA techniques. It was found that the paraffin binder decomposed into gaseous products at the temperature range of 250–320 °C and decomposition activation energies of 90-116 kJ/mol. Gonen et al. [39] reported the effects of zinc stearate addition on paraffin degradation using the DSC and TGA techniques. The paraffin decomposed more rapidly in an air environment than nitrogen.

Further, it was described that adding $ZnSt_2$ into paraffin significantly improved the rate of thermal degradation in air and nitrogen environments. In our previous study, it was found that the addition of aluminum into paraffin accelerated the decomposition and oxidation process, while the boron-loaded fuel samples exhibited higher heat release. Paraffin loaded with metallic additives can improve the peak exothermic temperature of combustion and net exothermicity [13,43]. The thermal reaction kinetics of paraffin-based fuels loaded with $LiAlH_4$ metal hydrides was examined by Boiocchi et al. [44], and the decomposition enthalpy of fuel improved with increasing the weight percentage of $LiAlH_4$ in formulations. Recently, Liu et al. [40] investigated the thermal reaction characteristics of paraffin in the presence of combustion catalysts such as catocene, copper chromite, and cobalt stearate. The decomposition and oxidation processes of paraffin were reported in single-stage, and two-dimensional diffusion (D2 model) was adopted as the kinetic model of the decomposition process. Further, it was shown that the cobalt stearate promoted paraffin decomposition, whereas copper chromite significantly favored paraffin oxidation and regression rates. Cerium oxide (CeO_2), also known as ceria, has been considered for potential heterogeneous catalysis because of its remarkable reactivity and redox properties [45–49]. It was revealed that by combining the CeO_2 with various metals, highly multifunctional catalytic composites could be produced, which can enhance the decomposition and oxidation process due to the synergistic metal-ceria interactions [50]. Therefore, this study examined the effect of CeO_2 combustion catalysts and Al additive on the thermal decomposition and combustion performance of paraffin-based fuels. The thermal reaction kinetics of paraffin were estimated through non-isothermal measurements using TGA experiments. Further, to assess the regression rates of prepared fuel formulation, the lab-scale ballistic tests were performed under an oxygen environment.

2. Experimental method

2.1. Material and solid fuel composition

Commercial grade paraffin wax (CAS Number: 8002-74-2) was used as a fuel binder, nano-size aluminum, called "Alex®" (CAS Number: 7429-90-5) of 30-40 nm particle size (as supplied by the manufacturer) and CeO_2 (CAS Number: 1306-38-3) of particle size < 30 nm were used as a fuel additive and catalyst, respectively. The properties of all materials procured in this study are listed in Table 1. Four fuel formulations were prepared: (S1) pure paraffin wax, used as a control sample; (S2) paraffin doped with 10 wt.% Al; (S3) paraffin doped with 10 wt.% CeO_2; and (S4) paraffin loaded with CeO_2-Al binary composite additives. The details of the prepared fuel samples are shown in Table 2.

Table 1
Properties of fuel matrix and additives

Properties	Paraffin	Aluminum	Cerium oxide
Chemical formula	$C_{31}H_{64}$	Al	CeO_2
Density (g/cm^3) at 25 °C	0.920	2.70	7.22
Melting point (°C)	59	660	2600
Particles size	pellets	30-40 nm	< 30 nm
Thermal conductivity (W/mK)	0.2-0.4	230	7-12

Table 2
Tested paraffin-based fuel formulations

Sample	Paraffin (wt.%)	Al (wt.%)	CeO_2 (wt.%)
Pure paraffin (S1)	100	-	-
10Al (S2)	90	10	-
10CeO_2 (S3)	90	-	10
10Al/10CeO_2 (S4)	80	10	10

2.2. Preparation of fuel samples

The ball milling, sol-gel method, and ultrasonic mixing techniques are frequently used to assemble nano thermites [51–54]. The sol-gel and ultrasonic techniques can demonstrate poor mixing at the nanoscale if the agglomeration of nanopowders is not broken up during ultrasonication. The ball milling method has shown great promise to produce binary composite powder and mature in technology that can be used for large-scale production of nano thermites [55,56]. The preparation of nano-thermite is very sensitive to experimental conditions such as vibration intensity, time, and process control agent (PCA) [51,53,55,56]. In this study, 10 wt.% CeO_2-Al binary composite powder was prepared by ball-milling CeO_2 and Al powders. The milling process was performed in a MM 400 RETSCH mixer mill using zirconia balls in a 50 mL stainless steel container filled with n-hexane as a PCA. During the ball milling, the vibration frequency was 50 Hz with an amplitude of 6.52 mm, and the average energy intensity was 0.75 W/g. The powder was milled for 10 h with a milling cycle of 60 min followed by 15 min in standby. In order to retrieve the evaporation of the PCA in the sample, PCA was added each time. The milling container was kept in an argon-filled glove box with O_2 and H_2O contents lower than 1 ppm to prevent the powders from oxidation. The prepared CeO_2-Al binary composite powder was maintained above the boiling temperature (69 °C) of the n-hexane for 2 hours to remove the PCA.

The solid fuels for thermal and ballistic tests were prepared by heating the paraffin wax to 80°C on a hot plate. The prepared CeO_2-Al binary composite powder was added to the hot molten paraffin wax, and the mixture was stirred for 15 min. Additives with large particle surfaces tend to aggregate and agglomerate in paraffin wax when conventional mixing is used. Sonication was employed to ensure homogeneous dispersion of the additives. The paraffin-additive mixture was sonicated for approximately 15 min. As a final step, the mixture was poured into the mold rapidly and in one movement to avoid the formation of air bubbles. After mixing the fuel sample, the mold was placed in the oven and cured at room temperature for 6 hours to remove air bubbles. In order to evaluate the quality of the prepared fuel sample, it was fractured and the surfaces were visually analyzed. It was observed that the prepared CeO_2-Al binary composite powder uniformly dispersed and completely densified solid without any voids, air bubbles, and other geometrical defects.

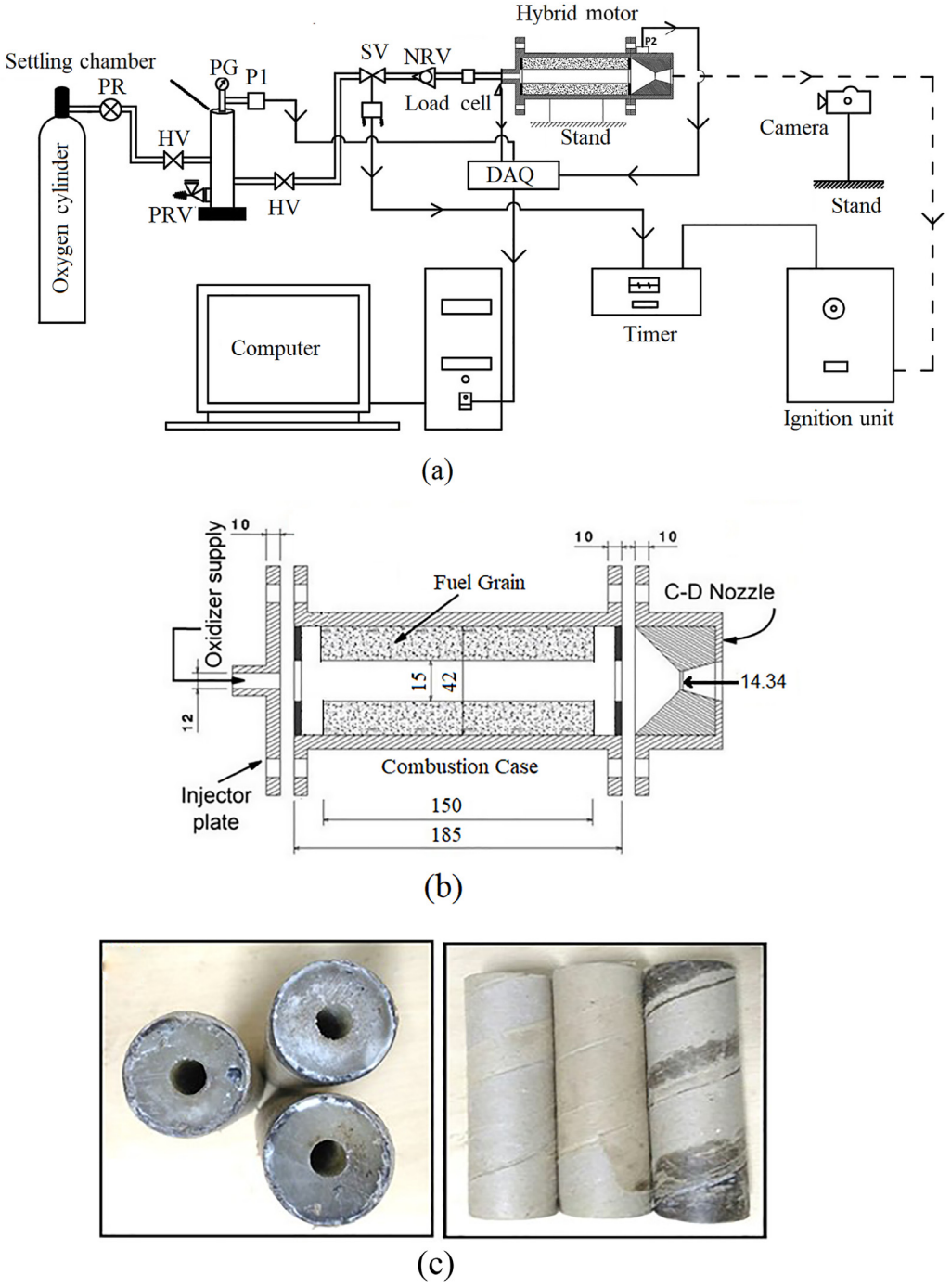

Fig. 1. (a) Schematic of hybrid rocket test facility. (b) Schematic of ballistic evaluation hybrid motor (all dimensions in mm). (c) Fabricated circular-port grains.

2.3. Characterization techniques

The microstructural study and phase evolution of the as-received and milled powders was characterized by an X-ray diffraction pattern using the DAVINCI instrument (BRUKER D8 Advance, USA), equipped with a copper target (Cu-Kα radiation 1.5418 Å) and scanning in the range of $2\theta = 10^{\circ}$ to 80°. The particle size distribution of as-received and post-milled powders was measured using Malvern/Nano ZS-90 (Malvern-PANalytical, Malvern, UK). Approximately 300 mg of powder was dispersed in ethanol, and measurements were performed with laser diffraction. The surface morphology elucidations of both as-received and milled powders were studied using a scanning electron microscope (SEM) JEOL JSM-6490LV (Jeol Ltd., Japan). The surface of the fuel samples was sputtered with Au-Pd to prevent overcharging. Using Spectrum Two Fourier transform infrared (FTIR) spectrometer (PerkinElmer, USA), the functional groups of fuel and binary composites were identified by scanning in the range 350–4000 cm^{-1} at a resolution of 4 cm^{-1}. The heat of combustion of fuel samples was evaluated using an isothermal bomb calorimeter (IKAC2000). In typical bomb calorimetry experiments, 1 g of fuel sample is burnt at an oxygen pressure of 2.5 MPa. Each fuel sample was tested three times, and the average value from the statistical analysis was presented for analysis. A thermogravimetric analyzer (TGA/DSC3+, Mettler-Toledo, Switzerland) was used to assess the degradation temperature and weight loss percentage of fuel samples. The 10 mg of fuel sample was used, and the low-temperature thermal decomposition carried out a 10 °C/min heating rate under an N_2 atmosphere. A bomb calorimeter, ParrModel 1108, manufactured by Parr Instrument Company, was used to measure the heat of combustion of

the paraffin-based solid fuels. The combustion bomb of the calorimeter is capable of withstanding a hydrostatic pressure of 20 MPa at room temperature. Nichrome ignition wire of known specific heat, 2.3 cal/cm, was used for sample ignition. A pellet press was used to compress the sample into a compact form to ensure the complete combustion of the sample. All the calorimetric experiments were performed under isothermal conditions.

2.4. Lab-scale ballistic tests

On a lab-scale static motor, a series of ballistic tests were performed with gaseous oxygen as the oxidizer. This test setup consists of a lab-scale rocket motor, thrust stand, oxidizer feed system, pyrogen igniter, and data acquisition system (Fig. 1(a)). Schematic of a lab-scale static hybrid motor is shown in Fig. 1(b). A hybrid motor has an oxidizer settling chamber measuring 33 mm long and 55 mm in diameter. A stainless-steel axial flow injector with a 47 mm pitch circle diameter was used to deliver the oxidizer into the combustion chamber. An igniter located at the head end of the motor will produce an initial heat source in the chamber that exceeds the ignition temperature of the fuel grain. In this process, the chamber is pre-heated, allowing the fuel to evaporate and react effectively with the oxygen. A combustion chamber of 150 mm in length and 42 mm inner diameter was designed to accommodate the fuel grain. A convergent-divergent nozzle with a 14.34 mm throat diameter, a 45° semi-convergent angle, and a 13° semi-divergent angle was used. A pressure regulator and a solenoid valve were used to control the oxidizer mass flow rate. An oxidizer mass flux range of 75.7 kg/(m^2·s) to 130.4 kg/(m^2·s) was used to test the fuel formulations. Fabricated fuel formulations are shown in Fig. 1(c). All the fuels were casted in single-port cylindrical grain configurations. A cylindrical hard-cardboard tube was used as a fuel mold. After the firing test, one can precisely remove the burned fuel grains from combustion chambers using cardboard tubes. The regression rate can be accurately predicted owing to the efficient removal of grain from the motor. The regression rate and fuel mass consumption were the post-test measurements.

A mass loss method was used to estimate the regression rate, which is the most accurate and widely used [31]. By using Eq. (1), we calculated the average regression rate for paraffin-based fuel.

$$\dot{r} = \frac{d_b - d_{ig}}{2t_b} \tag{1}$$

where d_b and d_{ig} are the diameter of the grain after combustion and before ignition, respectively. The t_b is the burning time between the start of the ignition process and the end of the oxidizer supply. The final fuel diameter was calculated using the following Eq. (2).

$$d_b = \sqrt{\left(d_{ig}^2 + \frac{m_b}{\frac{\pi}{4}\rho_f\, l_f}\right)} \tag{2}$$

Where ρ_f is solid fuel density, m_b indicates the burned mass of the fuel, and l_f represents the fuel length. The paraffin fuel droplets produced by the unstable molten liquid layer are not completely burned in the fuel port and ejected out the exhaust nozzle during combustion. As a result, the final unburned fuel mass uncertainty due to spilling of the unburned mass from the engine was roughly estimated to be 5% of the final fuel mass. The uncertainty in the measurement was evaluated based on the root-sum-square uncertainty rule [57]. The uncertainties in measurement are presented in Table 3. The regression rate and oxidizer mass flux uncertainties are found to be ±0.18 mm/s and ±4.6 kg/m^{2}s, respectively. The average oxidant mass flow was calculated according to Eq. (3)

$$G_{ox} = \frac{\dot{m}_{ox}}{A_p} \tag{3}$$

where A_p is the cross-sectional area of the fuel port and $\dot{m}_{ox}$ is the oxidizer mass flow rate. It was estimated by averaging the diameter of the post-combustion port and fuel port before ignition (Eq. (4))

$$A_P = \frac{\pi}{4}\left(\frac{d_b + d_{ig}}{2}\right)^2 \tag{4}$$

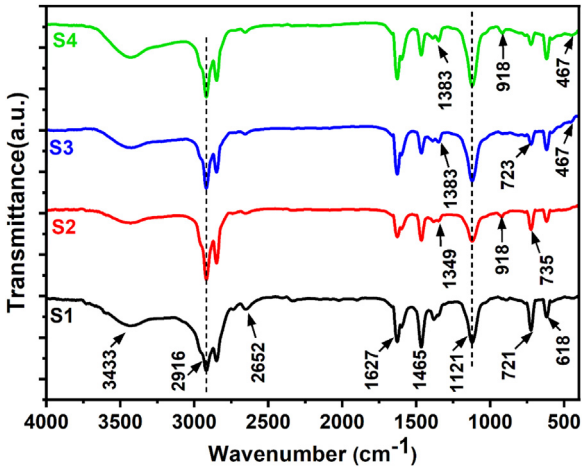

Fig. 2. FTIR spectra of paraffin-based fuels (S1-S4) doped with Al, CeO_2, and ball-milled CeO_2-Al binary composite.

3. Results and discussion

3.1. Characterization of the prepared materials

The FTIR spectra of paraffin and the CeO_2-Al-doped samples are shown in Fig. 2. From the FTIR spectrum, it is observed that the peak wavelength of paraffin wax did not significantly change when Al and CeO_2 particles were added. The spectra indicated the appearance of the bond peaks corresponding to the O-H stretching at approximately 3433 cm^{-1}, which is probably due to the adsorbed humidity. The absorption bands at 2916 cm^{-1} and 2890 cm^{-1} could be attributed to the strong symmetrical C-H stretching vibration and medium asymmetrical C-H stretching vibrations of alkanes, respectively. The peaks at 1627 cm^{-1} and 1121 cm^{-1} were ascribed to medium scissor vibration of the C-H bond and medium rocking skeleton vibration of the C-C bond, respectively. The absorption peaks at 721 cm^{-1} and 618 cm^{-1} were due to the rocking vibration of CH_2. These peaks appeared in all the paraffin-based samples doped with Al, CeO_2, and CeO_2-Al binary composite. As for the spectrum of S2, additional absorption peaks at 1349 cm^{-1} and 918 cm^{-1} were due to the characteristic Al-O stretching vibrations, whereas weak peaks (S3, S4) in the lower frequency region 467 cm^{-1} were identified of cerium–oxygen groups having a lower double-bond character and of Ce–O–Ce chains. The FTIR spectra confirm that the chemical reaction occurred between the CeO_2-Al and carbon of the paraffin matrix. Thus, adding Al and CeO_2 into paraffin showed good chemical compatibility and did not alter the chemical structure of paraffin. By using these FTIR spectra, vibrational changes can be detected as evidence of possible intermolecular interactions. There are interactions between the paraffin matrix and added additives when the peak intensity decreases, absorption peaks appear, or the appearance of new peaks.

Fig. 3 displays the XRD patterns of as received and milled powders. The characteristic peaks for CeO_2 nanoparticles located at 2θ = 28.2°, 32.2°, 47.2°, 55.8°, 58.6° and 75.7° were assigned to (111), (200), (220), (311), (222) and (400) lattice planes, respectively. The x-ray diffraction pattern of nAl powder shows two dominant peaks corresponding to the presence of aluminum. The diffraction peaks at 37.4°, 43.7°, 63°, and 76.9°, respectively, assigned to the (111), (200), (220), and (222) reflections of Face-Centered Cubic. The XRD patterns of CeO_2-Al binary composite powder after 10h milling time show broader diffraction peaks with low relative intensity. These peaks also confirms the phase transitions during the high-energy ball milling process. For the CeO_2-Al binary

Table 3
Measurement uncertainty analysis based on the root-sum-square uncertainty rule

Parameters	Uncertainty analysis	Uncertainty equation
[#]Regression rate($\dot{r}$)	±0.18 mm/s	$\zeta_r = \sqrt{[(\frac{\partial r}{\partial d_b}\zeta_{d_b})^2 + (\frac{\partial r}{\partial d_{ig}}\zeta_{d_{ig}})^2 + (\frac{\partial r}{\partial t_b}\zeta_{t_b})^2]}$
[###] Oxidizer mass flux (Gox)	±4.6 kg/(m^2·s)	$\zeta_{G_{ox}} = \sqrt{[(\frac{\partial r}{\partial \dot{m}_{ox}}\zeta_{\dot{m}_{ox}})^2 + (\frac{\partial r}{\partial A_p}\zeta_{A_p})^2]}$

[#] Where, $\zeta_r, \zeta_{d_b}, \zeta_{d_{ig}}$, and ζ_{t_b} are the uncertainty in the regression rate, burn port diameter, initial port diameter, and burn time, respectively.[###]Where, $\zeta_{G_{ox}}, \zeta_{\dot{m}_{ox}}$, and ζ_{A_p} are the uncertainty in the oxidizer mass flux, oxidizer mass flow, and port area, respectively.

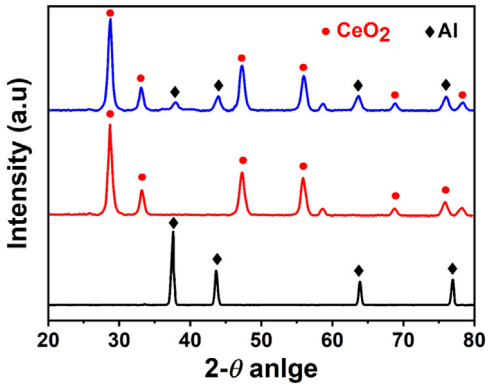

Fig. 3. X-ray diffraction patterns of as-received Al, CeO_2 particles, and ball-milled CeO_2-Al binary composite.

composite powder, the crystallinity decreased when compared with that of raw materials. This should have also resulted from the ball-milling since the mechanical energy from the friction of balls could transfer to the CeO_2-Al binary composite and affect its crystalline structure. In order to confirm the particle size of the additive and catalyst supplied by the manufacturer, the grain/crystallite size of these as-received and milled Nanoparticles was calculated using the Scherrer equation (Eq. (5)) based on the broadening of these peaks.

$$D = \frac{K_S \lambda}{(\cos\theta)\tau} \tag{5}$$

where D is the mean size of the crystalline, K_S is a shape factor constant in the range 0.8–1.2, λ is the X-ray wavelength, τ is peak width at FWHM, and θ is the Bragg angle. It was found that the average particle size of CeO_2 and Al was 28 nm and 35 nm, respectively. Similarly, the mean particle size of the CeO_2-Al binary composite was 25 nm after a milling time of 10 h.

Fig. 4(a)-(c) show SEM images of as-received and milled powder. As evidenced in Fig. 4(a) and (b), Al and CeO_2 powders exhibit spherical morphology with agglomeration that might occur due to magnetic interaction among nanoparticles. Some larger particles can be observed due to aggregation or overlapping of smaller particles. After 10 h of ball milling, the CeO_2-Al binary composite particle shape is almost spherical with a size less than 30 nm (Fig. 4(c)). However, due to the formation of agglomerates, no significant difference in size was found. Fig. 4(d) shows the histogram of the size distribution of as-received and milled particles. The broader peaks indicating aggregates of primary crystallites and mean particle size of Al, CeO_2, and CeO_2-Al obtained were approximately 34 nm, 29 nm, and 26 nm, respectively. This indicates that particle sizes obtained using Malvern/Nano ZS-90 are in good agreement with sizes calculated using the Scherrer equation. A ball milling process reduces agglomeration and particle size considerably, which in turn improves thermal decomposition kinetics and combustion performance.

3.2. Thermal decomposition and Kinetic Study

The thermal decomposition behavior of paraffin and CeO_2-Al doped paraffin samples were studied using TGA. The TG and corresponding DTG curves are shown in Fig. 5(a) and (b). The mass loss of S1, S2, S3, and S4 samples started at 260 °C, 251 °C, 242 °C, and 235 °C, and was completed at 404 °C, 398 °C, 377 °C, and 349 °C under an N_2 atmosphere at a heat rate of 10 °C/min. It suggested that Al, CeO_2, and CeO_2-Al binary composite have a positive effect on paraffin decomposition. Furthermore, the DTG curve in Fig. 5(b) shows that S3 and S4 samples have faster degradation and a higher decomposition rate than the pristine paraffin sample. The primary decomposition reaction of the S1 sample occurred between 270 °C and 400 °C and resulted in a mass loss of 97 percent. However, in the case of the paraffin sample doped with additives, the primary decomposition reaction accelerated at a low temperate range between 242 °C and 351 °C with a mass loss of 23 percent at the end of the decomposition reaction as reported in Table 4. However, the slow decomposition of pure paraffin may form high molecular weight hydrocarbons during the initial decomposition reaction. [40,41]. According to the maximum mass loss, paraffin could almost completely decompose into gas products. Furthermore, DTG curves of all tested samples show a single peak with the maximum rate of mass loss between 311-354 °C, confirming single-stage decomposition reactions (Fig. 5(b)). However, paraffin molecules have different chain lengths that behave similarly to most of the reactants under similar reaction conditions. When they are heated, they start to degrade into smaller chain lengths. At high temperatures, paraffin undergoes simultaneous pyrolysis and oxidation. Further, the decomposition products; alcohol, acid, aldehyde, and ketones are formed which complicate the decomposition/oxidation process.

The lower peak temperature of the DTG curve also indicates that the decomposition reactions are probably easier to proceed with the addition of nano Al and CeO_2 additives. Further, the chemical reaction between Al and CeO_2 may consist of the following two parts:

$$2Al + 3/2CeO_2 \rightarrow Al_2O_3 + 3/2Ce \tag{1}$$

$$2Al + 6CeO_2 \rightarrow Al_2O_3 + 3Ce_2O_3 \tag{2}$$

Al can react with the CeO_2, and form Al_2O_3 and Ce_2O_3 as products. Furthermore, the resulting Ce_2O_3 product most likely also has catalytic properties. These possible reactions also release heat and affect the combustion performance of the fuel grains. Thus, we have performed the isothermal heat of combustion tests as a pre-burning characterization to understand the effect of these additive combustion performances. The heat of combustion of the fuels was evaluated using pure oxygen as an oxidizer and the results are presented in Table 4. The average heat of combustion value for pure paraffin wax was found to be 41.28±1.1 MJ/kg and the addition of Al and CeO_2 to paraffin increased the heat of combustion. However, the S3 sample exhibited lower heat of combustion compared to the S4 sample, which can be attributed to the incomplete combustion of CeO_2 particles. The addition of Al into the paraffin matrix improved the thermodynamic characteristics (heat capacity and thermal conductivity), due to the uniform heating of the matrix. This can also be interpreted by the oxidation reactions, which produce intermetallic fuel compounds that react with the oxidizing gaseous species, and hence increase the temperature of the burning surface and accelerate the decomposition process [58]. Furthermore, if the mass of addi-

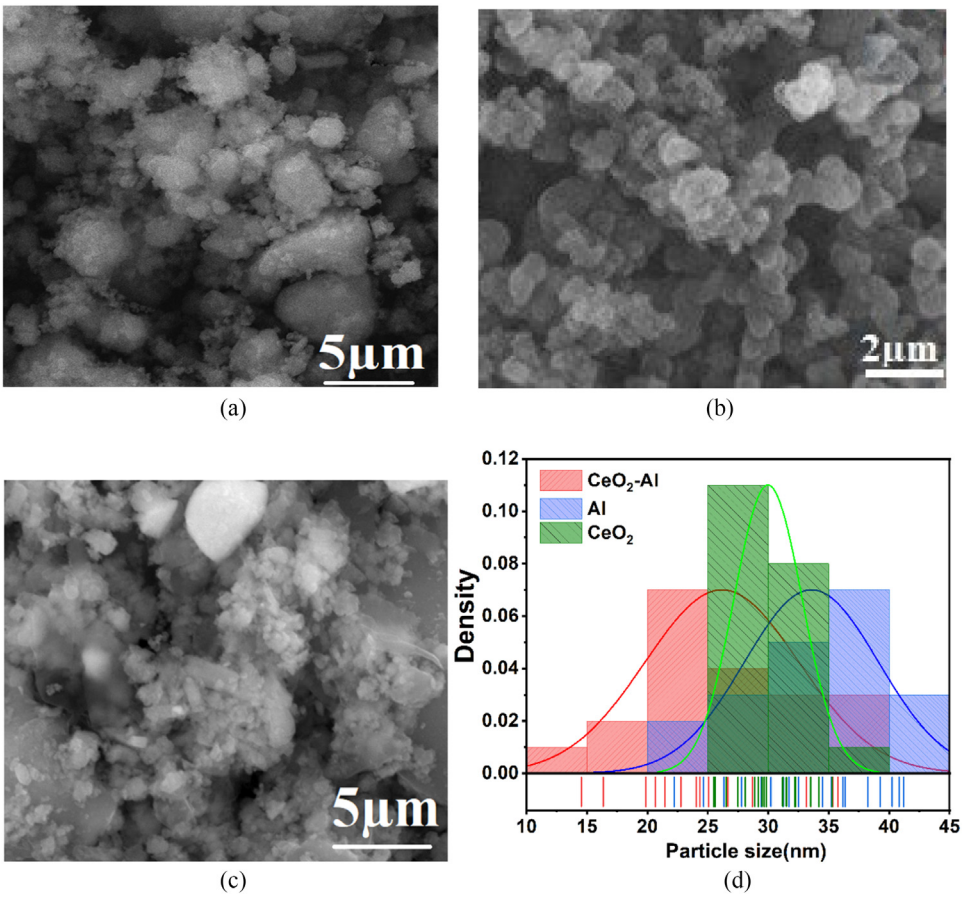

Fig. 4. SEM images of (a) as-received Al particles. (b) As-received CeO_2. (c) Ball-milled CeO_2-Al and (d) histogram of the size distribution of as-received and milled particles.

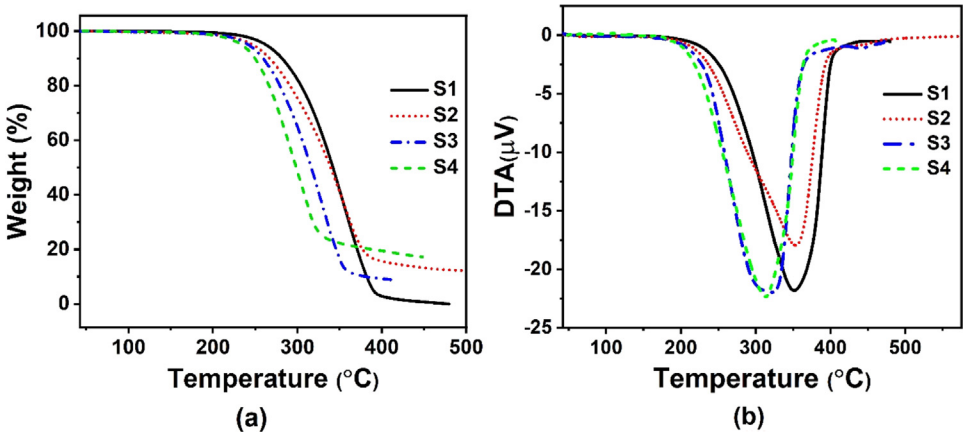

Fig. 5. (a) TGA and (b) DTG curves of paraffin-based fuels

Table 4
Thermal decomposition and kinetic parameters of the paraffin fuels under N_2 environment

Sample	Al/CeO_2 conc.	T_{onset} (°C)	T_{max} (°C)	E_a(kJ/mol)	ln(A) (min^{-1})	K (min^{-1})	Heat of combustion (MJ/kg)
S1	0:0	260	350	254	14.97	0.016	41.28±1.1
S2	10:0	251	354	242	14.43	0.015	44.50±1.2
S3	0:10	242	316	222	11.49	0.013	42.78±1.3
S4	10:10	235	311	214	10.24	0.011	45.41±1.2

tives in the fuel formulation is too large, the additives do not have time to warm up to the temperature of paraffin.

A mathematical model established by Coats-Redfern (CR) was used to evaluate the kinetic parameters (activation energy E_a and pre-exponential factor A) of thermal decomposition [59]. This method describes the relationship between the conversion rate of the reaction (α) and absolute temperature to calculate the kinetic parameters. The CR approach is widely considered a flexible method for determining thermal degradation mechanisms using TGA data. CR provides the following

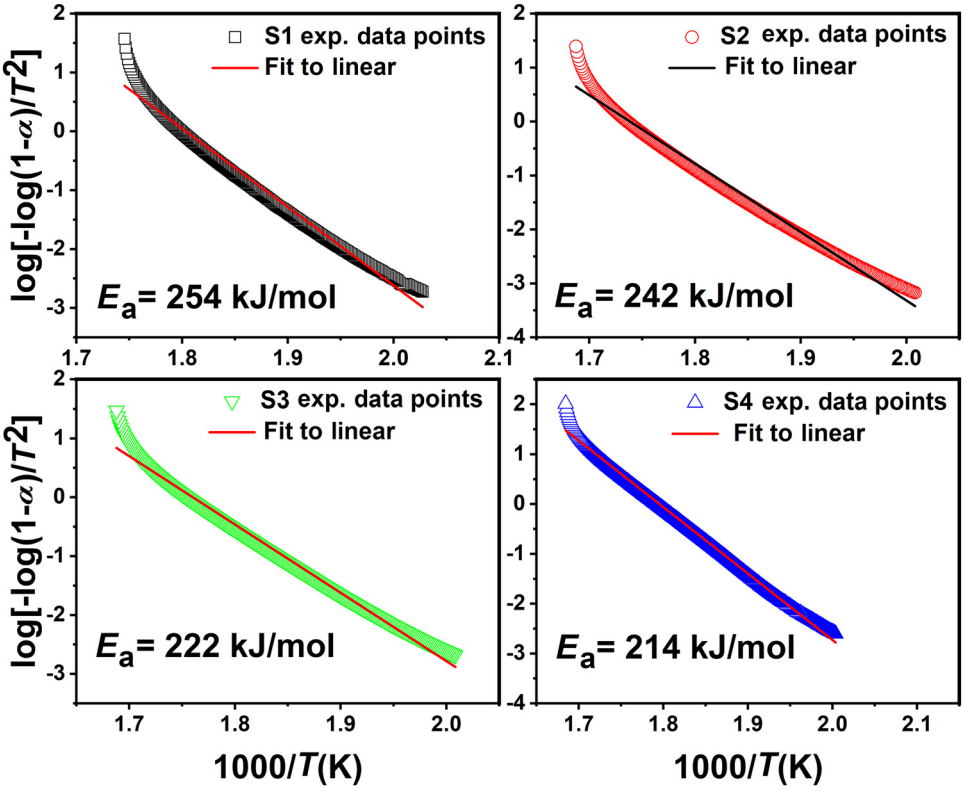

Fig. 6. Typical plots between log[-log(1-α)/T^2] versus (1/T) obtained for S1, S2, S3, and S4 samples using the Coats-Redfern model-fitting method.

correlation Eq. (6):

$$\ln\left(\frac{\beta}{T^2(1-2RT/E_a)}\right) = \ln\left(-\frac{AR}{E_a \ln(1-\alpha)}\right) - \frac{E_a}{RT} \quad (6)$$

For a fixed heating rate (β), the weight fraction conversion (α) is defined as Eq. (7):

$$\alpha = \frac{W_0 - W_t}{W_0 - W_\infty} \quad (7)$$

Where W_0, W_t, and W_∞ are the initial weight of the sample at a given temperature (or time t) and the final weight. The activation energy (E_a) and frequency factor (A) can be estimated from the plot between $\log(\frac{\beta}{T^2})$ and $1/T$, which yields a straight line with a high correlation coefficient.

The paraffin wax is a straight-chain hydrocarbon, and when exposed to heat, it starts to decompose into smaller chain lengths. The chain length can significantly alter the thermal decomposition kinetics when treated with metal ions catalysts [36,40]. The thermal decomposition kinetics of paraffin is assumed to be first-order reactions. Fig. 6 shows the plots between log[-log(1-α)/T^2] versus (1/T) obtained after fitting the experimental data to the integral kinetic function. The activation energy (E_a) for the single-step decomposition reaction was calculated from the slope given in Table 4. From experimental data fitting of E_a suggests that the correlation coefficients of all slopes were more than 0.99, which indicates the high reliability of TG data and the CR method. Table 4 represents the E_a obtained by the method mentioned above. It can be observed that the activation energy (E_a) was calculated in the range of 214–254 kJ/mol.

Interestingly, it may be noted that the activation energies of S2 -S4 samples decreased when nano Al additive and CeO_2 catalyst were added to the paraffin. The lower activation energy values indicate the early degradation kinetics of CeO_2-Al doped paraffin sample (S4), while the higher values of the activation energy observed with S1, and S2 samples indicate the decomposition of the paraffin matrix becomes fairly constrained by random chain scission process [60]. During the decomposition reactions, several high-weight hydrocarbons and porous compounds were formed, which could have catalyzed the decomposition of paraffin with autocatalytic reactions, resulting in the lower E_a. Polymer-based materials generally display such types of decomposition [38]. The pre-exponential factor (A) and rate constant (k) for the degradation of each sample were calculated using the intercept of the line drawn from experimental data using the CR method. The value of A, and k for the paraffin-based fuel is shown in Table 4. It was found that adding CeO_2 and Al into paraffin reduced the energy required to initiate the decomposition process. This is critical during the initial ignition phase of the combustion process, where the heating rate is minimal. It can also be noted that the addition of additive and catalyst slightly reduced the decomposition rate constants (k) and pre-exponential factor (A).

3.3. Regression rate study

On a lab-size ballistic hybrid motor, pure paraffin, paraffin with 10% Al, and CeO_2 fuel samples were burned in GOX under a range of oxidizer mass fluxes (69.13–132.86 kg/m^{2}s) and pressures (0.59–0.89 MPa). Fig. 7 shows the average regression rates vs. average oxidizer mass flux of paraffin-based fuel. The solid lines indicate the model fit of regression rate data to a power-law approximation using the least-squares regression method. The regression rate exponents ($\dot{r} = aG_{ox}^n$) for each set of fuel formulations are evaluated and given in Table 5. The addition of the additives to paraffin resulted in relatively higher exponent values (n = 0.34-0.39), indicating that the paraffin-based fuel displays a similar regression rate behavior as the oxidizer mass flux increases. The value of oxidizer mass flux in classical diffusion-limited theories is reported as 0.8 [5], which is significantly higher than the value observed in paraffin-based formulation (n = 0.34-0.39). The paraffin fuel loaded with binary composite CeO_2-Al exhibited a regression rate increase of approximately 1.49 mm/s over the baseline (1.03 mm/s) at oxidizer mass fluxes of 132 kg/(m^2·s). On the other hand, at oxidizer mass fluxes (> 95 kg/(m^2·s)), the fuel grain loaded with Al additive (S2) and CeO_2 catalyst (S3) outperforms compared to the pure fuel sample. It can be observed that the addition of 10 wt.% of CeO_2 and Al into paraffin has reasonably improved the regression rate. In the case of S3 sample, at a low

Table 5
Regression rate results of paraffin-based fuels under an oxygen environment

Fuel sample	Average chamber pressure (MPa)	Initial mass of fuel (kg)	Final mass of fuel (kg)	Oxidizer mass flux gox, (kg/(m^2·s))	Regression rate (mm/s)	Regression rate exponents	
						a	*n*
S1	0.72	0.64	0.49	70.76	1.03	0.235±0.01	0.34±0.02
	0.69	0.61	0.45	81.59	1.11		
	0.81	0.66	0.41	103.16	1.19		
	0.72	0.54	0.32	125.22	1.27		
S2	0.71	0.66	0.29	71.68	1.1	0.23±0.02	0.37±0.01
	0.62	0.62	0.35	84.42	1.22		
	0.76	0.68	0.37	102.21	1.34		
	0.88	0.69	0.27	132.66	1.4		
S3	0.66	0.52	0.22	69.13	1.12	0.245±0.02	0.35±0.03
	0.59	0.66	0.25	81.81	1.15		
	0.81	0.68	0.23	104.23	1.31		
	0.76	0.67	0.31	130.14	1.38		
S4	0.74	0.62	0.24	71.68	1.15	0.215±0.01	0.39±0.02
	0.89	0.59	0.30	84.42	1.28		
	0.82	0.67	0.31	102.21	1.39		
	0.78	0.65	0.28	132.86	1.49		

Initial port diameter = 30 mm; fuel grain length = 150 mm; burn time = 5.5 s.

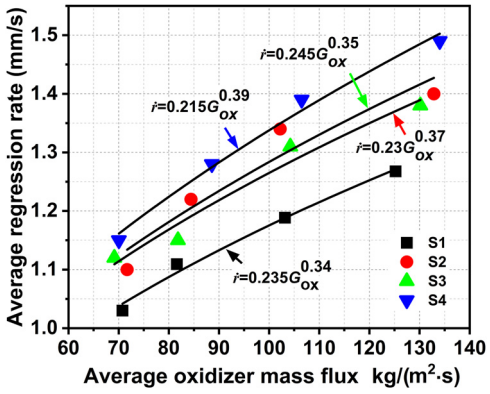

Fig. 7. Comparison of average regression rate for various paraffin samples with additives.

oxidizer mass flux range (69.13-81.81 kg/(m^2·s)), the regression rate increased in the range of 1.12-1.15 mm/s compared to that of pure paraffin (1.03-1.11 mm/s), whereas 1.31 mm/s and 1.38 mm/s improvement was seen with intermediate flux (90-100 kg/(m^2·s)) and highest oxidizer mass flux (101-130 kg/(m^2·s)), respectively. Whereas the regression rate of the S2 sample increased in the range of 1.1 mm/s to 1.22 mm/s at the low oxidizer mass flux range (71.68-84.42 kg/(m^2·s)), and an improvement of 1.34 mm/s to 1.4 mm/s was observed at an intermediate flux (85-102.2 kg/(m^2·s)) and highest oxidizer mass flux (103-132.66 kg/(m^2·s)), respectively compared to pure paraffin. Therefore, the regression rate enhancement can be ascribed to the improved catalytic activity of CeO_2 with paraffin. Stephens et al. [36] showed that adding nanoscale TiO_2 and CeO_2 catalytic additives in composite propellants enhanced the burn rate performance.

The addition of CeO_2 improves the oxidation rate of the paraffin fuel matrix, forming a large number of active species and, as a result, improves the regression rate performance [36,61,62]. Nano CeO_2 has significant potential due to its demonstrated success as an effective oxidizing catalyst [63]. In the combustion process, CeO_2 particles undergo numerous reactions before leaving the flame zone rather than being consumed. During the oxidation process, the CeO_2 donated oxide ions which facilitated further oxidation of Al. As a result of the transportation of reactive oxygen ions from CeO_2 oxidizer to Al fuel, a large amount of heat was released which ultimately improved the regression rate of fuel. During combustion, paraffin fuel develops a liquid film on the fuel surface [34]. The increased Re number can enhance the diffusion of paraffin droplets from the liquid surface layer at higher oxidizer fluxes, leading to enhanced fuel mass transfer by droplet entrainment. Unstable wavelets form on the liquid surface when an oxidizer stream flows over a thin, low-viscosity liquid layer, creating tiny paraffin droplets rolling up at the edge of the surface. These droplets are entrained with Al and CeO_2 particles and burnt in the combustion zone with oxidizer flow. With the entrainment of liquid droplets, the low-viscosity and unstable liquid layer promote additional mass transfer to the combustion zone [31]. The presence of Al particles in the combustion zone can enhance the radiative heat transfer, the heat of oxidation, and adiabatic flame temperature, which can ultimately enhance the specific impulse of a hybrid rocket [3,4,64–66]. Al can speed up the regression rate by releasing a significant amount of energy during oxidation.

However, the regression rate of CeO_2 doped paraffin grain (S3) is lower than that of the Al-based fuel (S2) sample. This could be due to the fact that the Al melts around 660 °C and CeO_2 melts around 2600 °C, and during the combustion process, the CeO_2 melting phase could inhibit better heat transfer and result in lower performance. Under the same operating condition, the regression rate of the tested paraffin fuel loaded with binary composite CeO_2-Al (S4) shows a similar enhancement trend. The released oxygen from CeO_2 makes the liquid-solid phase oxidation reaction and combustion more complete. At the same time, the released oxygen may react with the excess Al powder and release significant heat (as we can observe from Table 4, S4 has the highest heat release). The regression rate was improved from 1.28 mm/s at the low oxidizer mass flux (71.68-80 kg/(m^2·s)), to 1.39 mm/s at the intermediate flux range (92-102.21 kg/(m^2·s)) and to 1.49 mm/s calculated at the highest oxidizer flux (103-132 kg/(m^2·s)) when compared to pure paraffin (1.03 -1.11 mm/s). It is evident that the catalytic and synergetic effect of CeO_2-Al additives (S4 sample) is most prominent at high oxidizer mass flux.

4. Conclusions

this study focuses on the thermal decomposition kinetics and combustion performance of paraffin-based fuel in the presence of CeO_2 catalyst and Al additive. The paraffin-based fuels were manufactured using a typical melt-cast technique. Paraffin decomposition was positively affected by adding Al, CeO_2, and CeO_2-Al binary composite additives. Fuel samples with additive and catalyst exhibited faster degradation and a higher decomposition rate than the pristine paraffin sample. The kinetic model of decomposition suggests that the addition of CeO_2 and Al into paraffin reduced the amount of energy (E_a: S1>S2>S3>S4) required to initiate the decomposition process. It is also observed that adding additive and catalyst slightly reduced the decomposition rate constants (k) and pre-exponential factor (A). The overall decomposition

reaction profile displayed single decomposition steps of paraffin-based fuel, and more complex chemical kinetic modeling is needed to describe the reaction mechanism of these prepared fuels. The lab-scale ballistic tests showed that the average regression rate of paraffin-Al (S2) and paraffin-CeO_2(S3) samples increased in the range of 1.1-1.4 mm/s and 1.12-1.38 mm/s, respectively, whereas, with the CeO_2-Al binary composite (S4) sample, a reasonable improvement in the range of 1.15-1.49 mm/s was reported. The regression rate enhancement can be ascribed to the improved catalytic activity of CeO_2 and enhanced radiative heat transfer due to the presence of Al in the combustion zone. The kinetics committee of the International Confederation for Thermal Analysis and Calorimetry (ICTAC) recently advised the use of a single heating method to calculate kinetic parameters. Therefore, the kinetic studies of paraffin-based fuel in the presence of CeO_2 catalyst and Al additive are to be performed at various heating rates would be part of future study to compare to the existing results.

Declaration of Competing Interest

The authors declare that they have no known competing financial interests or personal relationships that could have appeared to influence the work reported in this paper.

Acknowledgments

The authors gratefully acknowledge the Hindustan Institute of Technology and Science for their support and experimental facilities. Additionally, the authors thank the Centre for Clean Energy and Nano Convergence (CENCON), for providing the SEM facilities.

References

[1] C. Paravan, L. Galfetti, R. Bisin, F. Piscaglia, Combustion Processes in Hybrid Rockets, Int. J. Energ. Mater. Chem. Propuls 18 (2019) 255–286, doi:10.1615/IntJEnergeticMaterialsChemProp.2019027834.
[2] W.H. Knuth, M.J. Chiaverini, J.A. Sauer, D.J. Gramer, Solid-Fuel Regression Rate Behavior of Vortex Hybrid Rocket Engines, J. Propuls. Power. 18 (2002) 600–609, doi:10.2514/2.5974.
[3] L. Galfetti, L. Merotto, M. Boiocchi, F. Maggi, L.T. DeLuca, Experimental investigation of paraffin-based fuels for hybrid rocket propulsion, EUCASS Proc. Ser. – Adv. Aerosp. Sci 4 (2013) 59–74, doi:10.1051/eucass/201304059.
[4] A. Sossi, E. Duranti, M. Manzoni, C. Paravan, L.T. DeLuca, A.B. Vorozhtsov, M.I. Lerner, N.G. Rodkevich, A.A. Gromov, N. Savin, Combustion of HTPB-Based Solid Fuels Loaded with Coated Nanoaluminum, Combust. Sci. Technol. 185 (2013) 17–36, doi:10.1080/00102202.2012.707261.
[5] M.J. Chiaverini, N. Serin, D.K. Johnson, Y.-C. Lu, K.K. Kuo, G.A. Risha, Regression Rate Behavior of Hybrid Rocket Solid Fuels, J. Propuls. Power. 16 (2000) 125–132, doi:10.2514/2.5541.
[6] S. Kim, H. Moon, J. Kim, J. Cho, Evaluation of Paraffin–Polyethylene Blends as Novel Solid Fuel for Hybrid Rockets, J. Propuls. Power. 31 (2015) 1750–1760, doi:10.2514/1.B35565.
[7] Y. Pal, K.H. Kumar, Y.-H. Li, Ballistic and mechanical characteristics of paraffin-based solid fuels, CEAS Space J 11 (2019) 317–327, doi:10.1007/s12567-019-00250-2.
[8] T. Matsuoka, K. Kamei, Y. Nakamura, H. Nagata, Modified Regression Rate Formula of PMMA Combustion by a Single Plane Impinging Jet, Int. J. Aerosp. Eng. 2017 (2017) 1–9, doi:10.1155/2017/6485757.
[9] Y. Pal, S.N. Mahottamananda, S.K. Palateerdham, S. Subha, A. Ingenito, Review on the regression rate-improvement techniques and mechanical performance of hybrid rocket fuels, FirePhysChem 1 (2021) 272–282, doi:10.1016/j.fpc.2021.11.016.
[10] M.Z. Akhter, M.A. Hassan, Ballistic and thermomechanical characterization of paraffin-based hybrid rocket fuels loaded with light metal hydrides, Acta Astronaut 178 (2021) 370–381, doi:10.1016/j.actaastro.2020.09.015.
[11] J.H. Corpening, R.K. Palmer, S.D. Heister, J.J. Rusek, Combustion of advanced nontoxic hybrid propellants, International Journal of Alternative Propulsion 1 (2007) 154–173, doi:10.1504/IJAP.2007.013018.
[12] C. Carmicino, A.Russo Sorge, Experimental Investigation into the Effect of Solid-Fuel Additives on Hybrid Rocket Performance, J. Propuls. Power. 31 (2015) 699–713, doi:10.2514/1.B35383.
[13] Y. Pal, V.R. Kumar, Physical and Ballistic Characterization of Aluminum-Loaded Paraffin Hybrid Rocket Fuels, Energy Fuels 31 (2017) 10133–10143, doi:10.1021/acs.energyfuels.7b01636.
[14] Paravan, Nano-Sized, and Mechanically Activated Composites: Perspectives for Enhanced Mass Burning Rate in Aluminized Solid Fuels for Hybrid Rocket Propulsion, Aerospace 6 (2019) 127, doi:10.3390/aerospace6120127.
[15] F. Maggi, G. Gariani, L. Galfetti, L.T. DeLuca, Theoretical analysis of hydrides in solid and hybrid rocket propulsion, Int. J. Hydrog. Energy. 37 (2012) 1760–1769, doi:10.1016/j.ijhydene.2011.10.018.
[16] R. Bisin, C. Paravan, S. Alberti, L. Galfetti, A new strategy for the reinforcement of paraffin-based fuels based on cellular structures: The armored grain — Mechanical characterization, Acta Astronaut 176 (2020) 494–509, doi:10.1016/j.actaastro.2020.07.003.
[17] T. Kato, N. Hashimoto, H. Nagata, I. Kudo, A Preliminary Study of End-Burning Hybrid Rocket: Part 1 Combustion Stability, J. Jpn. Soc. Aeronaut. SPACE Sci. 49 (2001) 33–39, doi:10.2322/jjsass.49.33.
[18] H. Nagata, M. Ito, T. Maeda, M. Watanabe, T. Uematsu, T. Totani, I. Kudo, Development of CAMUI hybrid rocket to create a market for small rocket experiments, Space Inspir. Humankind Sel. Proc. 56th Int. Astronaut. Fed. Congr. Fukuoka Jpn. 59 (2006) 253–258 17-21 Oct. 2005, doi:10.1016/j.actaastro.2006.02.031.
[19] T. Matsuoka, K. Kamei, Y. Nakamura, H. Nagata, Modified Regression Rate Formula of PMMA Combustion by a Single Plane Impinging Jet, Int. J. Aerosp. Eng. 2017 (2017) 6485757, doi:10.1155/2017/6485757.
[20] S. Kim, J. Lee, H. Moon, J. Kim, H. Sung, O.C. Kwon, Regression Characteristics of the Cylindrical Multiport Grain in Hybrid Rockets, J. Propuls. Power. 29 (2013) 573–581, doi:10.2514/1.B34619.
[21] A. Bath, Performance Characterization of Complex Fuel Port Geometries for Hybrid Rocket Fuel Grains, (n.d.) 69.
[22] D.J. Vonderwell, I.F. Murray, S.D. Heister, Optimization of hybrid-rocket-booster fuel-grain design, J. Spacecr. Rockets. 32 (1995) 964–969, doi:10.2514/3.26716.
[23] G. Cai, H. Zhu, D. Rao, H. Tian, Optimal design of hybrid rocket motor powered vehicle for suborbital flight, Aerosp. Sci. Technol. 25 (2013) 114–124, doi:10.1016/j.ast.2011.12.014.
[24] B. Ahn, H. Kang, E. Lee, Y. Yun, S. Kwon, Design of Multiport Grain with Hydrogen Peroxide Hybrid Rocket, J. Propuls. Power. 34 (2018) 1189–1197, doi:10.2514/1.B36949.
[25] M. Dinesh, R. Kumar, Experimental Studies of Protrusion-Inserted Hybrid Rocket Motor with Varying L/D Ratio, J. Spacecr. Rockets. 58 (2021) 134–147, doi:10.2514/1.A34759.
[26] M. Dinesh, S.S. Rajput, R. Kumar, Protrusion effect on the performance of hybrid rocket with liquefying and non-liquefying fuels, Acta Astronaut 178 (2021) 536–547, doi:10.1016/j.actaastro.2020.09.039.
[27] M. Dinesh, R. Kumar, Utility of Multiprotrusion as the Performance Enhancer in Hybrid Rocket Motor, J. Propuls. Power. 35 (2019) 1005–1017, doi:10.2514/1.B37491.
[28] C. Lee, Y. Na, J.-W. Lee, Y.-H. Byun, Effect of induced swirl flow on regression rate of hybrid rocket fuel by helical grain configuration, Aerosp. Sci. Technol. 11 (2007) 68–76, doi:10.1016/j.ast.2006.07.006.
[29] S.A. Whitmore, S.D. Walker, Engineering Model for Hybrid Fuel Regression Rate Amplification Using Helical Ports, J. Propuls. Power. 33 (2017) 398–407, doi:10.2514/1.B36208.
[30] E. Paccagnella, F. Barato, D. Pavarin, A. Karabeyoğlu, Scaling Parameters of Swirling Oxidizer Injection in Hybrid Rocket Motors, J. Propuls. Power. 33 (2017) 1378–1394, doi:10.2514/1.B36241.
[31] M.A. Karabeyoglu, D. Altman, B.J. Cantwell, Combustion of Liquefying Hybrid Propellants: Part 1, General Theory, J. Propuls. Power. 18 (2002) 610–620, doi:10.2514/2.5975.
[32] D.S. Maki, N.K. Nemer, S.M. Uosof, S.N. Mohi, Use of Nano Chemical Additives to Improve the Properties of Industrial Used Paraffin Wax, Iraqi J. Sci. 0 (2019) 99–104.
[33] M. Boiocchi, P. Milova, L. Galfetti, L. Di Landro, A.K. GolovkoM. Calabro, L. DeLuca, S. Frolov, L. Galfetti, O. Haidn (Eds.), A wide characterization of paraffin-based fuels mixed with styrene-based thermoplastic polymers for hybrid propulsion, Prog. Propuls. Phys., EDP Sciences (2016) 241–262, doi:10.1051/eucass/201608241.
[34] M.A. Karabeyoglu, B.J. Cantwell, Combustion of Liquefying Hybrid Propellants: Part 2, Stability of Liquid Films, J. Propuls. Power. 18 (2002) 621–630, doi:10.2514/2.5976.
[35] S.N. Mahottamananda, N.P. Kadiresh, Y. Pal, Regression Rate Characterization of HTPB-Paraffin Based Solid Fuels for Hybrid Rocket, Propellants Explos. Pyrotech. 45 (2020) 1755–1763, doi:10.1002/prep.202000051.
[36] M.A. Stephens, E.L. Petersen, R. Carro, D.L. Reid, S. Seal, Multi-Parameter Study of Nanoscale TiO_2 and CeO_2 Additives in Composite AP/HTPB Solid Propellants, Propellants Explos. Pyrotech. 35 (2010) 143–152, doi:10.1002/prep.200800104.
[37] X. Mao, L. Jiang, C. Zhu, X. Wang, Effects of Aluminum Powder on Ignition Performance of RDX, HMX, and CL-20 Explosives, Adv. Mater. Sci. Eng. 2018 (2018) 1–8, doi:10.1155/2018/5913216.
[38] Kh.G.K. Singh, S. Halder, S. Pati, J. Wang, Microencapsulation of Paraffin Wax Microspheres with Silver, Def. Sci. J. 68 (2018) 218, doi:10.14429/dsj.68.11410.
[39] M. Gönen, D. Balköse, F. İnal, S. Ülkü, The effect of zinc stearate on thermal degradation of paraffin wax, J. Therm. Anal. Calorim. 94 (2008) 737–742, doi:10.1007/s10973-008-9365-8.
[40] L. Liu, Z. Ji, Y. Deng, S. Hu, Thermal reaction characteristics of paraffin in the presence of combustion catalysts, Thermochim. Acta. 695 (2021) 178836, doi:10.1016/j.tca.2020.178836.
[41] K.-S. Jaw, C.-K. Hsu, J.-S. Lee, The thermal decomposition behaviors of stearic acid, paraffin wax and polyvinyl butyral, Mater. Characterization Therm, Anal. Methods. (2001) 165–168 367–368, doi:10.1016/S0040-6031(00)00680-8.
[42] G.P. Santos, P.T. Lacava, S.R. Gomes, J.A.F.F. Rocco, Kinetics Parameters Evaluation of Paraffin-Based Fuel, in: IMECE2012, Volume 1. Advances in Aerospace Technology, 2012: pp. 471-480. doi:10.1115/IMECE2012-86275.
[43] Y. Pal, V.R. Kumar, Thermal Decomposition Study of Paraffin Based Hybrid Rocket Fuel containing Aluminum and Boron additives, Thermochim. Acta. (2017), doi:10.1016/j.tca.2017.06.002.
[44] M. Boiocchi, L. Galfetti, L. Di Landro, Preliminary Kinetic Characterization of Lithium–Aluminum Based Hydrides for Airbreathing Propulsion, J. Propuls. Power. 34 (2018) 48–57, doi:10.2514/1.B36307.

[45] R. Agnihotri, C. Oommen, Cerium oxide based active catalyst for hydroxylammonium nitrate (HAN) fueled monopropellant thrusters, RSC Adv 8 (2018) 22293–22302, doi:10.1039/C8RA02368A.
[46] J. Shi, H. Wang, Y. Liu, X. Ren, H. Sun, B. Lv, Rapid microwave-assisted hydrothermal synthesis of CeO2 octahedra with mixed valence states and their catalytic activity for thermal decomposition of ammonium perchlorate, Inorg. Chem. Front. 6 (2019) 1735–1743, doi:10.1039/C9QI00362B.
[47] N. Yadav, P.K. Srivastava, M. Varma, Recent advances in catalytic combustion of AP-based composite solid propellants, Def. Technol. 17 (2021) 1013–1031, doi:10.1016/j.dt.2020.06.007.
[48] Mei Deqing, Li Xianming, Wu Qimin, Sun Ping, Role of Cerium Oxide Nanoparticles as Diesel Additives in Combustion Efficiency Improvements and Emission Reduction, J. Energy Eng. 142 (2016) 04015050, doi:10.1061/(ASCE)EY.1943-7897.0000329.
[49] H. Jung, D.B. Kittelson, M.R. Zachariah, The influence of a cerium additive on ultrafine diesel particle emissions and kinetics of oxidation, Combust. Flame. 142 (2005) 276–288, doi:10.1016/j.combustflame.2004.11.015.
[50] M. Konsolakis, M. Lykaki, Facet-Dependent Reactivity of Ceria Nanoparticles Exemplified by CeO2-Based Transition Metal Catalysts: A Critical Review, Catalysts 11 (2021) 452, doi:10.3390/catal11040452.
[51] D. Sundaram, V. Yang, R.A. Yetter, Metal-based nanoenergetic materials: Synthesis, properties, and applications, Prog. Energy Combust. Sci. 61 (2017) 293–365, doi:10.1016/j.pecs.2017.02.002.
[52] R.A. Yetter, G.A. Risha, S.F. Son, Metal particle combustion and nanotechnology, Proc. Combust. Inst. 32 (2009) 1819–1838, doi:10.1016/j.proci.2008.08.013.
[53] D. Xu, Y. Yang, H. Cheng, Y.Y. Li, K. Zhang, Integration of nano-Al with Co3O4 nanorods to realize high-exothermic core–shell nanoenergetic materials on a silicon substrate, Combust. Flame. 159 (2012) 2202–2209, doi:10.1016/j.combustflame.2012.01.022.
[54] D. Stamatis, E.L. Dreizin, K. Higa, Thermal Initiation of Al-MoO3 Nanocomposite Materials Prepared by Different Methods, J. Propuls. Power. 27 (2011) 1079–1087, doi:10.2514/1.B34179.
[55] S. Wang, X. Liu, M. Schoenitz, E.L. Dreizin, Nanocomposite Thermites with Calcium Iodate Oxidizer, Propellants Explos. Pyrotech. 42 (2017) 284–292, doi:10.1002/prep.201600213.
[56] Q. Nguyen, C. Huang, M. Schoenitz, K.T. Sullivan, E.L. Dreizin, Nanocomposite thermite powders with improved flowability prepared by mechanical milling, Powder Technol 327 (2018) 368–380, doi:10.1016/j.powtec.2017.12.082.
[57] J.R. Taylor, Introduction To Error Analysis: The Study of Uncertainties in Physical Measurements, 2nd edition, University Science Books, Sausalito, 1997.
[58] F. Chalghoum, D. Trache, M. Benziane, A. Benhammada, Effect of micro- and nano-CuO on the thermal decomposition kinetics of high-performance aluminized composite solid propellants containing complex metal hydrides, Prog. Solid Rocket Propuls 2 (2022) 36–49, doi:10.1016/j.fpc.2022.03.007.
[59] A.W. Coats, J.P. Redfern, Kinetic Parameters from Thermogravimetric Data, Nature 201 (1964) 68–69, doi:10.1038/201068a0.
[60] T. Rogaume, Thermal decomposition and pyrolysis of solid fuels: Objectives, challenges and modelling, Fire Saf. J. 106 (2019) 177–188, doi:10.1016/j.firesaf.2019.04.016.
[61] H. Liu, Y. Huang, X. Wang, R. Lu, Effect of CeO2 on High-Temperature Oxidation Performance of Electron Beam Cladding NiCoCrAlY Coating on Ni-Based Alloy, Adv. Mater. Sci. Eng. 2020 (2020) 8731315, doi:10.1155/2020/8731315.
[62] V. Bambagioni, C. Bianchini, Y. Chen, J. Filippi, P. Fornasiero, M. Innocenti, A. Lavacchi, A. Marchionni, W. Oberhauser, F. Vizza, Energy Efficiency Enhancement of Ethanol Electrooxidation on Pd–CeO2/C in Passive and Active Polymer Electrolyte-Membrane Fuel Cells, ChemSusChem 5 (2012) 1266–1273, doi:10.1002/cssc.201100738.
[63] C. Korsvik, S. Patil, S. Seal, W.T. Self, Superoxide dismutase mimetic properties exhibited by vacancy engineered ceria nanoparticles, Chem. Commun. (2007) 1056–1058, doi:10.1039/B615134E.
[64] P. Tadini, C. Paravan, L.T. DeLuca, Ballistic Characterization of Metallized HTPB-based Fuels with Swirling Oxidizer in Lab-Scale Hybrid Burner, (n.d.) 10.
[65] L.T. DeLuca, L. Galfetti, F. Maggi, G. Colombo, L. Merotto, M. Boiocchi, C. Paravan, A. Reina, P. Tadini, L. Fanton, Characterization of HTPB-based solid fuel formulations: Performance, mechanical properties, and pollution, Acta Astronaut 92 (2013) 150–162, doi:10.1016/j.actaastro.2012.05.002.
[66] S. Chen, Y. Tang, W. Zhang, R. Shen, H. Yu, Y. Ye, L.T. DeLuca, Innovative Methods to Enhance the Combustion Properties of Solid Fuels for Hybrid Rocket Propulsion, Aerospace 6 (2019) 47, doi:10.3390/aerospace6040047.